Chinese Chemical Letters 34 (2023) 107494

Contents lists available at ScienceDirect

Chinese Chemical Letters

journal homepage: www.elsevier.com/locate/cclet

Boosting Li-ion storage in Li_2MnO_3 by unequal-valent Ti^{4+}-substitution and interlayer Li vacancies building

Yu Tian[a,1], Yuling Zhao[b,1], Fanqi Meng[d,1], Kaicheng Zhang[a], Yanyuan Qi[a], Yujie Zeng[a], Congcong Cai[a], Yuli Xiong[a,e], Zelang Jian[a,*], Yang Sun[b,c,*], Lin Gu[d,*], Wen Chen[a]

[a] School of Materials Science and Engineering Key Laboratory of Advanced Technology for Materials Synthesis and Processing, Wuhan University of Technology, Wuhan 430070, China
[b] School of Materials, Shenzhen Campus of Sun Yat-sen University, Shenzhen 518107, China
[c] 21C Innovation Laboratory, Contemporary Amperex Technology Ltd. (CATL), Ningde 352100, China
[d] Institute of Physics, Chinese Academy of Sciences, Beijing 100190, China
[e] Sanya Science and Education Innovation Park of Wuhan University of Technology, Wuhan 430070, China

ARTICLE INFO

Article history:
Received 7 February 2022
Revised 10 March 2022
Accepted 7 May 2022
Available online 11 May 2022

Keywords:
Lithium-ion batteries
Li_2MnO_3
Unequal-valent Ti^{4+}-substitution
Interlayer Li vacancies
Activated $Mn^{3+/4+}$ redox

ABSTRACT

Lithium rich layered oxide (LRLO) has been considered as one of the promising cathodes for lithium-ion batteries (LIBs). The high voltage and large capacity of LRLO depend on Li_2MnO_3 phase. To ameliorate the electrochemical performance of Li_2MnO_3, also written as $Li(Li_{1/3}Mn_{2/3})O_2$, we propose a strategy to substitute Mn^{4+} and Li^+ in Mn/Li transition metal layer with Ti^{4+}, which can stabilize the structure of Li_2MnO_3 by inhibiting the excessive oxidation of O^{2-} above 4.5 V. More significantly, the unequal-valent substitution brings about the emergence of interlayer Li vacancies, which can promote the Li-ion diffusion based on the enlarged interlayer and increase the capacity by activating the $Mn^{3+/4+}$ redox. We designed $Li_{0.7}[Li_{1/3}Mn_{2/3}]_{0.7}Ti_{0.3}O_2$ with high interlayer Li vacancies, which presents a high capacity (290 mAh/g at 10 mA/g) and stable cycling performance (84% over 60 cycles at 50 mA/g). We predict that this strategy will be helpful to further improve the electrochemical performance of LRLOs.

The continuous expanding application field of lithium-ion batteries (LIBs) brings about an urgent demand for high-energy-density and long-life LIBs [1–3]. Recently, lithium rich layered oxide materials (LRLOs) have received significant attention due to their large capacity and high redox potential. LRLOs can be formularized as $xLi_2MnO_3{\cdot}(1-x)LiMO_2$ ($0 < x < 1$), where Li_2MnO_3 is a special $LiMO_2$ transition metal (TM) layered oxide with one-third of the TM replaced by Li [4–6]. The ultra-high capacity of LRLOs results from the extra Li^+ sited in Li_2MnO_3 ingredient, which can be activated with lattice oxygen oxidation when charging above 4.5 V [7–9]. However, the removal of Li^+ in TM layer of Li_2MnO_3 is laborious in dynamics [10], and excessive Li^+ deficiency easily suffers structural destruction, such as TM migration [11] and oxygen dimerization ($O^{2-} \rightarrow O^{n-}$) [12], leading to poor rate performance and serious LRLOs degeneration both in capacity and voltage [13]. As mentioned, Li_2MnO_3 is a pivotal component and plays as the main "contributor" in LRLOs, but Li_2MnO_3 itself has bad electrochemical activity and faces severe electrochemical deterioration [14].

Although many strategies, such as atomic doping [15–17], atomic mixing [18,19] and surface coating [20,21], are effective for LRLOs and other cathode materials to keep their high energy densities during the cycling, it is still hard to greatly improve the electrochemical performance of monoclinic Li_2MnO_3. Many efforts have been reported to deeply understand the decay mechanism of Li_2MnO_3, introducing that the primary reasons are oxygen release and subsequent structural destruction caused by the excessive oxygen oxidation at high voltages [22,23]. So far, unmodified Li_2MnO_3 cathode has bad capacity retention even within 30 cycles, and it can only operate at a very low current density below 20 mA/g [24–27]. Xia's group used Li_2RuO_3 as a model and designed a Li/Ru disorganized TM layer, which restrained oxygen release and alleviated the cathode deterioration, providing a new strategy to improve the stability of Li_2MnO_3 [19]. Yabuuchi's group prepared a $xLi_2TiO_3(1-x)LiMnO_2$ binary system, which could deliver a reversible capacity of ~250 mAh/g even at a high x value of 0.75, indicating that titanium anchored in Li_2MO_3 structure could

* Corresponding authors.
E-mail addresses: zelangjian@whut.edu.cn (Z. Jian), sunyang5@mail.sysu.edu.cn (Y. Sun), l.gu@iphy.ac.cn (L. Gu).
[1] These authors contributed equally to this work.

https://doi.org/10.1016/j.cclet.2022.05.008
1001-8417/

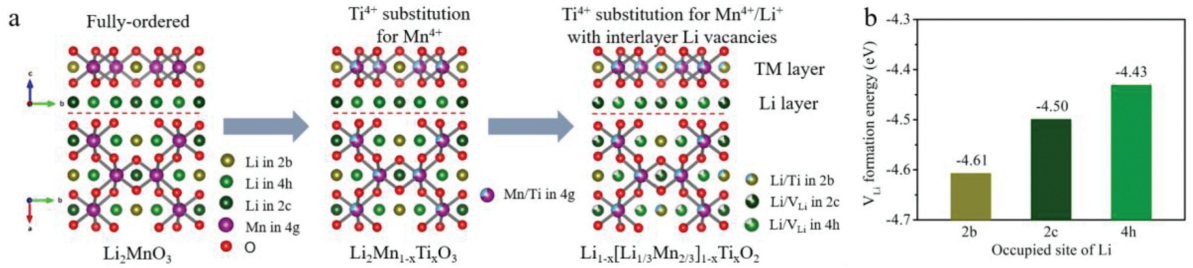

Fig. 1. Design of unequal-valent Ti^{4+}-substitution $Li_{1-x}[Li_{1/3}Mn_{2/3}]_{1-x}Ti_xO_2$ with interlayer Li vacancies. (a) The atomic structure evolution from fully ordered Li_2MnO_3 (left) to equal-valent Ti^{4+} substituted $Li_2Mn_{1-x}Ti_xO_3$ (middle), and then to unequal-valent Ti^{4+} substituted $Li_{1-x}[Li_{1/3}Mn_{2/3}]_{1-x}Ti_xO_2$ with interlayer vacancies (right). (b) The theoretical calculation results of vacancy (Li) formation energy in Li_2MnO_3.

improve its electrochemical properties [28]. Ti^{4+} can replace Mn^{4+} and Li^+ in the TM layer and help improve the capacity retention of Li_2MnO_3 cathode because of the same octahedral configuration and electrochemical inertness of Ti^{4+} at high voltages [29–32]. In addition to Ti^{4+}-substitution, another effective strategy to improve electrochemical performance is to introduce vacancies in cathodes, which can optimize the electronic properties of host materials, facilitating charge transfer and redox kinetics for Li-ion storage [33,34]. In the case of cation vacancies, it can also serve as extra host sites for Li-ions insertion, promoting Li-ion diffusion kinetics during charge/discharge processes [35].

In this work, we designed Li_2MnO_3 cathodes with Ti^{4+} substitution for Mn^{4+}/Li^+ in TM layer accompanied by vacancies in lithium layer to improve the electrochemical performance. According to the density functional theory (DFT) calculation, Ti^{4+} substitution for Li^+ in the TM layer results in partial interlayer Li loss due to the unequal chemical valence of Ti^{4+} and Li^+, simultaneously improving the kinetic activity of Li-ion diffusion. The designed $Li_{0.7}[Li_{1/3}Mn_{2/3}]_{0.7}Ti_{0.3}O_2$ cathode shows high capacity, stable cycling performance and enhanced rate capability, which delivers a capacity of 290 mAh/g (229 mAh/g for Li_2MnO_3) at 10 mA/g and a capacity of 242 mAh/g (167 mAh/g for Li_2MnO_3) with capacity retention of 84% (39% for Li_2MnO_3) after 60 cycles at 50 mA/g. The improved electrochemical performance of $Li_{0.7}[Li_{1/3}Mn_{2/3}]_{0.7}Ti_{0.3}O_2$ cathode benefits from the unequal-valent substitution of Ti^{4+} for Mn^{4+}/Li^+ and the associated interlayer Li vacancies, which inhibits the excessive oxidation of O^{2-} above 4.5 V, promotes Li-ion diffusion kinetics and activates the reversible redox reaction of $Mn^{3+/4+}$. The unequal-valent substitution of Ti^{4+} is an effective strategy to improve the electrochemical performance of Li_2MnO_3.

The structure of Li_2MnO_3 originates from α-$NaFeO_2$ and presents monoclinic structure with space group C2/m [36]. As shown in Fig. 1a (left), the fully ordered Li_2MnO_3 can be regarded as a TM layered oxide with the chemical formula of $Li[Li_{1/3}Mn_{2/3}]O_2$, and the ordered TM slab is composed of one-third $[Li_{2b}O_6]$ and two-thirds $[Mn_{4g}O_6]$ octahedrons. We follow the design rules described in Fig. 1a. Ti^{4+} can efficiently replace Mn^{4+} on the 4g site because of the similar radius and same valence state of Ti^{4+} and Mn^{4+} ions. $[Ti_{4g}O_6]$ can inhibit the excessive oxidation of O^{2-} above 4.5 V and improve the cyclic stability of Li_2MnO_3 structure due to the electrochemical inertness of Ti^{4+} at high voltage. Based on equivalent state substitution $Li_2Mn_{1-x}Ti_xO_3$, we can adjust the ratio of lithium and titanium sources to make Ti^{4+} substitute Li^+ on the 2b site and form Li vacancies in lithium layer, represented by a general stoichiometry of $Li_{1-x}[Li_{1/3}Mn_{2/3}]_{1-x}Ti_xO_2$. The formation of Li vacancies is caused by the unequal-valent substitution between Ti^{4+} and Li^+. And the amount of Li vacancies grows with the increase of the unequal-valent Ti^{4+}-substitution. Introduction of Li vacancy will promote the Li-ion diffusion and activate the reversible redox reaction of $Mn^{3+/4+}$ during charging/discharging processes, leading to high Li^+ storage ability.

However, Li vacancy probably emerges at three sites of 2b, 2c and 4h. The theoretical calculation for each lithium-absence-state indicates that Li vacancy between TM layer is determined by the energetically favorable configuration. According to the simulation results, Li-ions would be preferentially extracted out from lithium layer. For the case of the first Li-ion extraction, the energetically favorable sites are 4h and 2c positions for both pure Li_2MnO_3 and Ti^{4+} substituted Li_2MnO_3. The formation of a Li vacancy in the $LiMn_2$ layer (TM layer) requires 0.18 eV higher energy than that in the lithium layer (Fig. 1b). It suggests that Li^+ preferentially anchored at 2b site in TM layer in crystallization process, emerging Li vacancies mainly at 2c and 4h sites in lithium layer [37].

The $Li_{1-x}[Li_{1/3}Mn_{2/3}]_{1-x}Ti_xO_2$ can be easily synthesized by solid-phase reaction. Specifically, the prepared materials are $Li_{0.9}[Li_{1/3}Mn_{2/3}]_{0.9}Ti_{0.1}O_2$, $Li_{0.7}[Li_{1/3}Mn_{2/3}]_{0.7}Ti_{0.3}O_2$, $Li_{0.5}[Li_{1/3}Mn_{2/3}]_{0.5}Ti_{0.5}O_2$, which can be rewritten as $Li_{0.9}[(Li_{0.9}Ti_{0.1})_{1/3}(Mn_{0.9}Ti_{0.1})_{2/3}]O_2$, $Li_{0.7}[(Li_{0.7}Ti_{0.3})_{1/3}(Mn_{0.7}Ti_{0.3})_{2/3}]O_2$, and $Li_{0.5}[(Li_{0.5}Ti_{0.5})_{1/3}(Mn_{0.5}Ti_{0.5})_{2/3}]O_2$, respectively. The inductively coupled plasma (ICP) results of these prepared materials are shown in Fig. 2a, which are in good agreement with their chemical formula. The particle morphology was characterized by scanning electron microscopy (SEM). As shown in Figs. 2b-e, all samples have the similar primary particle size of 2–3 μm *via* solid-phase synthesis. One difference observed from SEM images is that the primary particles of $Li_{0.5}[Li_{1/3}Mn_{2/3}]_{0.5}Ti_{0.5}O_2$ locally agglomerate and form secondary particles (Fig. S1 in Supporting information).

To confirm the atomic arrangement of the above designed materials, we conducted high-angle annular bright field-scanning transmission electron microscopy (HAABF-STEM). Fig. 2f shows the HAABF-STEM image of $Li_{0.9}[Li_{1/3}Mn_{2/3}]_{0.9}Ti_{0.1}O_2$ along the [100] zone axis. The atomic arrangement of $Li_{0.9}[Li_{1/3}Mn_{2/3}]_{0.9}Ti_{0.1}O_2$ is similar to that of C2/m Li_2MnO_3 with a layer spacing of 4.8 Å and a repeating sequence of two-atom TM–TM dumbbells in TM layer [36]. A few (002) plane slip is caused by the partial absence of interlayer Li. In the HAABF-STEM image of $Li_{0.7}[Li_{1/3}Mn_{2/3}]_{0.7}Ti_{0.3}O_2$ along the [100] zone axis (Fig. 2g), most regular domains with consecutive superlattice planes and the enclosed domains (red dotted lines) with continuous TM atoms coexist, indicating that the partial Li atoms at 2b sites are replaced by Mn or Ti atoms. In addition, the spacing distance of $Li_{0.7}[Li_{1/3}Mn_{2/3}]_{0.7}Ti_{0.3}O_2$ expands to 4.9 Å. Fig. 2h displays a HAABF-STEM image of $Li_{0.5}[Li_{1/3}Mn_{2/3}]_{0.5}Ti_{0.5}O_2$ along the [110] orientation. Interestingly, the atomic arrangement of $Li_{0.5}[Li_{1/3}Mn_{2/3}]_{0.5}Ti_{0.5}O_2$ likes the structure of a spinel phase [38], which is quite different from the atomic arrangement of Li_2MnO_3. By the way, the $Li_{0.5}[Li_{1/3}Mn_{2/3}]_{0.5}Ti_{0.5}O_2$ with less Li content can be written as $Li[Li_{1/3}Mn_{2/3}Ti]O_4$ resembling spinel-phase $LiMn_2O_4$.

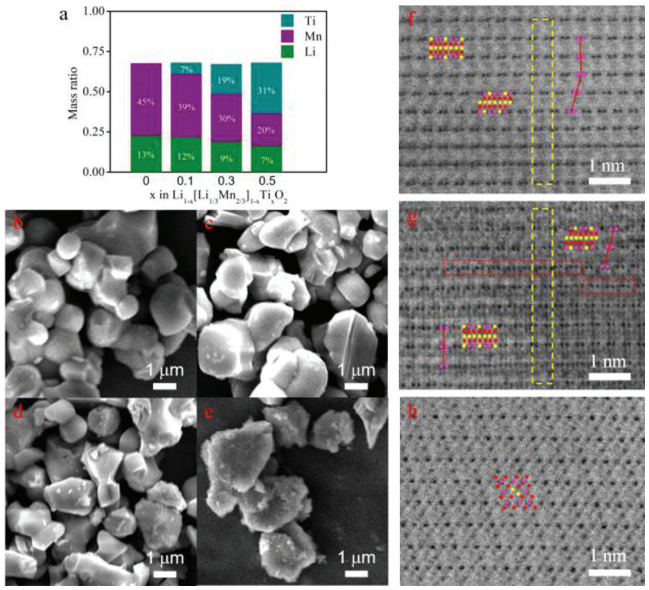

Fig. 2. (a) The ICP results of the prepared $Li_{1-x}[Li_{1/3}Mn_{2/3}]_{1-x}Ti_xO_2$ ($x=0$, 0.1, 0.3 and 0.5). The SEM images of (b) Li_2MnO_3, (c) $Li_{0.9}[Li_{1/3}Mn_{2/3}]_{0.9}Ti_{0.1}O_2$, (d) $Li_{0.7}[Li_{1/3}Mn_{2/3}]_{0.7}Ti_{0.3}O_2$, and (e) $Li_{0.5}[Li_{1/3}Mn_{2/3}]_{0.5}Ti_{0.5}O_2$. The HAABF-STEM images along the [100] zone axis for (f) $Li_{0.9}[Li_{1/3}Mn_{2/3}]_{0.9}Ti_{0.1}O_2$, (g) $Li_{0.7}[Li_{1/3}Mn_{2/3}]_{0.7}Ti_{0.3}O_2$ and [110] zone axis for (h) $Li_{0.5}[Li_{1/3}Mn_{2/3}]_{0.5}Ti_{0.5}O_2$. Yellow dashed boxes in (f, g) indicate the same nine layers in $Li_{0.9}[Li_{1/3}Mn_{2/3}]_{0.9}Ti_{0.1}O_2$ and $Li_{0.7}[Li_{1/3}Mn_{2/3}]_{0.7}Ti_{0.3}O_2$. The ball represents atom in (f-h). Pink: Mn/Ti; Yellow: Li; Red: O.

The structures of $Li_{1-x}[Li_{1/3}Mn_{2/3}]_{1-x}Ti_xO_2$ ($x=0$, 0.1, 0.3 and 0.5) were detected by X-ray diffractometer (XRD) and Raman spectroscopy measurements. Fig. 3a shows the XRD patterns of $Li_{1-x}[Li_{1/3}Mn_{2/3}]_{1-x}Ti_xO_2$, and all strong diffraction peaks are similar to the layered α-$NaFeO_2$ structure. The 2θ around 20°–22° is attributed to the superlattice plane in monoclinic Li_2MnO_3, corresponding to (020) and (110) planes [39]. The superlattice peaks become weak with the augment of the x values, which reflects a growing tendency to shape a chaotic arrangement of atoms (Mn/Ti/Li) in TM layer. Finally, the superlattice diffraction peaks disappear in $Li_{0.5}[Li_{1/3}Mn_{2/3}]_{0.5}Ti_{0.5}O_2$ with spinel structure. As shown in the enlarged XRD patterns at 18°–23° (Fig. 3b) and 35°–40° (Fig. 3c), the low-2θ-shift of (001) and (130) diffraction peaks corresponds to the increase of the interplanar spacing, which fits well with the HAABF-STEM images (Figs. 2f and g) and the XRD-rietveld results (Fig. S2 and Table S1 in Supporting information), indicating increased Li vacancies in $Li_{0.9}[Li_{1/3}Mn_{2/3}]_{0.9}Ti_{0.1}O_2$ and $Li_{0.7}[Li_{1/3}Mn_{2/3}]_{0.7}Ti_{0.3}O_2$. Moreover, a new diffraction peak (indexed to (311) plane in spinel $LiMn_2O_4$ [40]) is observed in $Li_{0.9}[Li_{1/3}Mn_{2/3}]_{0.9}Ti_{0.1}O_2$ and $Li_{0.7}[Li_{1/3}Mn_{2/3}]_{0.7}Ti_{0.3}O_2$ (Fig. 3c), ascribed to the interlayer Li vacancies.

Raman shift (Fig. 3d) was used to analyze the molecular structures of $Li_{1-x}[Li_{1/3}Mn_{2/3}]_{1-x}Ti_xO_2$, which were difficult to be detected by XRD measurements. In monoclinic Li_2MnO_3, there are two strong stretching-vibration (A_{1g} and A_g) peaks and a distinct bending-vibration (E_g) peak [41]. Specifically, the A_g peak located at 425 cm^{-1} stands for a characteristic vibration of monoclinic Li_2MnO_3 structure [42], while E_g and A_{1g} peaks at 487 cm^{-1} and 605 cm^{-1} are associated with the Raman-sensitive layered structure [43]. For spinel-phase $Li_{0.5}[Li_{1/3}Mn_{2/3}]_{0.5}Ti_{0.5}O_2$, the A_g vibration disappears and the A_{1g} peak shifts to 630 cm^{-1}, which is obviously different from the monoclinic Li_2MnO_3 structure [44]. For $Li_{0.9}[Li_{1/3}Mn_{2/3}]_{0.9}Ti_{0.1}O_2$ and $Li_{0.7}[Li_{1/3}Mn_{2/3}]_{0.7}Ti_{0.3}O_2$, a slight red shift of A_{1g} peak indicates that they tend to transform to spinel phase [45]. However, the stretching A_g vibrations still exist in their molecular structures, illustrating that they still contain the monoclinic structure (like Li_2MnO_3). The E_g peak gradually weakens because of the variations in the local vibration symmetry of [TMO_6] octahedron [46], which mainly generates by the Li vacancies and Ti^{4+} substitutions.

X-ray photoelectron spectroscopy (XPS) was employed to identify valence states of Mn and Ti in these materials. As shown in Figs. 3e and f, both Mn and Ti present as tetravalence in $Li_{0.9}[Li_{1/3}Mn_{2/3}]_{0.9}Ti_{0.1}O_2$ and $Li_{0.7}[Li_{1/3}Mn_{2/3}]_{0.7}Ti_{0.3}O_2$, which indirectly proves the existence of Li vacancies. By the way, a right-shoulder peak visualizes at the Mn $2p_{3/2}$ spectra of $Li_{0.5}[Li_{1/3}Mn_{2/3}]_{0.5}Ti_{0.5}O_2$, indicating the co-existence of Mn^{4+} and Mn^{3+} in spinel-phase $Li_{0.5}[Li_{1/3}Mn_{2/3}]_{0.5}Ti_{0.5}O_2$.

The charge/discharge measurements of $Li_{1-x}[Li_{1/3}Mn_{2/3}]_{1-x}Ti_xO_2$ ($x=0$, 0.1, 0.3 and 0.5) were conducted to explore the influence of the unequal-valent Ti^{4+}-substitution with interlayer Li vacancies on the electrochemical performance. Figs. 4a-d display the charge/discharge curves of the above cathode materials for the first two cycles at a current density of 10 mA/g. To facilitate comparison, their initial charge/discharge curves are placed together in Fig. S3 (Supporting information). The initial charge capacities of Li_2MnO_3 (247 mAh/g), $Li_{0.9}[Li_{1/3}Mn_{2/3}]_{0.9}Ti_{0.1}O_2$ (231 mAh/g) and $Li_{0.7}[Li_{1/3}Mn_{2/3}]_{0.7}Ti_{0.3}O_2$ (205 mAh/g) are mainly contributed by the oxidation of O^{2-} above 4.5 V. With the increase of unequal-valent Ti^{4+}-substitution, the decrease of the charging capacity is ascribed to the effort of Ti^{4+} substitution, which inhibits the lattice oxygen oxidation at high voltages. Meanwhile, the slightly increasing capacity between 3.5–4.5 V is caused by the oxidation of Mn^{3+}. By contrast, the spinel-phase $Li_{0.5}[Li_{1/3}Mn_{2/3}]_{0.5}Ti_{0.5}O_2$ cathode exhibits much lower first charge capacity (117 mAh/g) than other samples. The initial discharge capacities of Li_2MnO_3, $Li_{0.9}[Li_{1/3}Mn_{2/3}]_{0.9}Ti_{0.1}O_2$, $Li_{0.7}[Li_{1/3}Mn_{2/3}]_{0.7}Ti_{0.3}O_2$, and $Li_{0.5}[Li_{1/3}Mn_{2/3}]_{0.5}Ti_{0.5}O_2$ cathodes are 229, 241, 290 and 252 mAh/g, respectively. Compared with Li_2MnO_3, the Ti^{4+}-substituted samples present a new plateau, located at around 2.8 V in $Li_{0.9}[Li_{1/3}Mn_{2/3}]_{0.9}Ti_{0.1}O_2$ and $Li_{0.7}[Li_{1/3}Mn_{2/3}]_{0.7}Ti_{0.3}O_2$, but 2.6 V in spinel-phase $Li_{0.5}[Li_{1/3}Mn_{2/3}]_{0.5}Ti_{0.5}O_2$. This unique lithiation process is related to the reduction of Mn^{4+} accompanying with the intercalation of Li^+ [18], which benefits from interlayer Li vacancies. The plateau related to $Mn^{3+/4+}$ redox extends with the unequal-valent Ti^{4+} substitution, increasing until the phase transferred to spinel after Ti^{4+} substituted Li_2MnO_3. The long plateau means a deep reduction reaction of $Mn^{3+/4+}$, indicating that unequal-valent Ti^{4+}-substitution and interlayer Li vacancies can increase the capacity of the sample. And the voltages associated with the increased capacities of $Li_{0.9}[Li_{1/3}Mn_{2/3}]_{0.9}Ti_{0.1}O_2$ and $Li_{0.7}[Li_{1/3}Mn_{2/3}]_{0.7}Ti_{0.3}O_2$ are completely retained in the second cycle, indicating good reversibility of $Mn^{3+/4+}$ redox. The corresponding differential capacity versus voltage (dQ/dV) plots of $Li_{1-x}[Li_{1/3}Mn_{2/3}]_{1-x}Ti_xO_2$ ($x=0$, 0.1, 0.3 and 0.5) exhibit similar electrochemical changes to their charge/discharge curves. Fig. 4e shows initial dQ/dV plots of charging process, the oxygen dimerization peak weakens with the increase of x value and finally disappears in spinel-phase $Li_{0.5}[Li_{1/3}Mn_{2/3}]_{0.5}Ti_{0.5}O_2$. The paired dQ/dV plots during discharge are shown in Fig. 4f, a sharp peak emerges around 2.8 V after unequal-valent Ti^{4+} substituting, which corresponds to the $Mn^{3+/4+}$ redox activated by Ti^{4+} substitution and interlayer Li vacancies. The sharpest reduction peak appears in $Li_{0.7}[Li_{1/3}Mn_{2/3}]_{0.7}Ti_{0.3}O_2$, and the reduction peak shifts to 2.6 V in spinel-phase $Li_{0.5}[Li_{1/3}Mn_{2/3}]_{0.5}Ti_{0.5}O_2$.

To further understand the contribution of interlayer Li vacancies caused by unequal-valent Ti^{4+}-substitution to Li-ion storage, we compare the electrochemical characteristics of equal-valent Ti^{4+} substituted $Li_2Mn_{1-x}Ti_xO_3$, including $Li_2Mn_{0.9}Ti_{0.1}O_3$ and $Li_2Mn_{0.7}Ti_{0.3}O_3$, where Ti^{4+} only replaces Mn^{4+} without Li vacancy formation. The XRD patterns of $Li_2Mn_{1-x}Ti_xO_3$ ($x=0$,

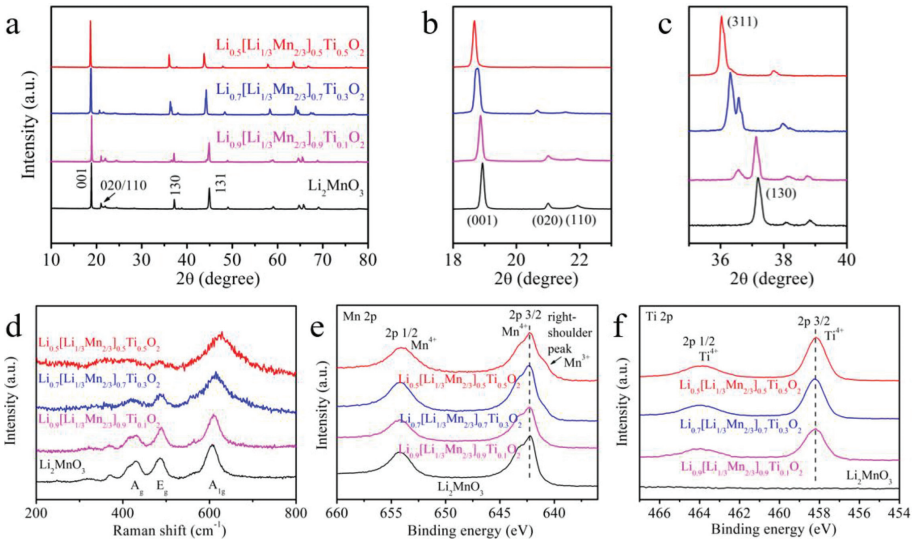

Fig. 3. (a-c) XRD patterns at different ranges, (d) Raman shifts and (e, f) high-resolution XPS spectra for Mn and Ti of $Li_{1-x}[Li_{1/3}Mn_{2/3}]_{1-x}Ti_xO_2$ ($x = 0$, 0.1, 0.3 and 0.5).

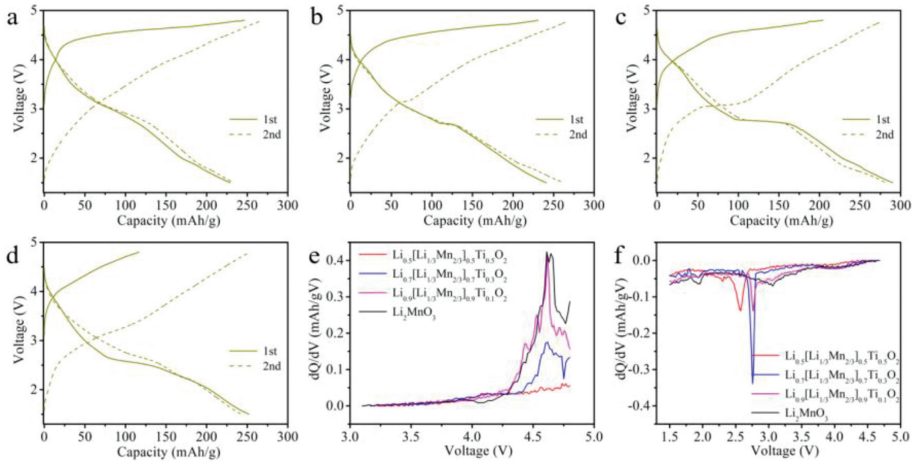

Fig. 4. First-two cycles charge/discharge curves of (a) Li_2MnO_3, (b) $Li_{0.9}[Li_{1/3}Mn_{2/3}]_{0.9}Ti_{0.1}O_2$, (c) $Li_{0.7}[Li_{1/3}Mn_{2/3}]_{0.7}Ti_{0.3}O_2$, and (d) $Li_{0.5}[Li_{1/3}Mn_{2/3}]_{0.5}Ti_{0.5}O_2$ at 10 mA/g. The corresponding dQ/dV plots of (e) charging process and (f) discharging process related to the first cycle.

0.1 and 0.3) (Fig. S4 in Supporting information) manifest high similar structure. Fig. S5 (Supporting information) shows their charge/discharge curves at 10 mA/g. The simply equal-valent Ti^{4+}-substitution (Ti substituted Mn) can also activate $Mn^{3+/4+}$ redox, but reversibility is worse than that of unequal-valent Ti^{4+}-substituted Li_2MnO_3, which is our designed strategy to achieve Ti^{4+}-substitution and build interlayer Li vacancies. The $Li_2Mn_{0.9}Ti_{0.1}O_3$ and $Li_2Mn_{0.7}Ti_{0.3}O_3$ show the lower Coulombic efficiency (CE) than that of $Li_{0.9}[Li_{1/3}Mn_{2/3}]_{0.9}Ti_{0.1}O_2$ and $Li_{0.7}[Li_{1/3}Mn_{2/3}]_{0.7}Ti_{0.3}O_2$ in the second cycle, indicating that interlayer Li vacancies can also improve the stability of electrochemical process. Compared with the designed unequal-valent Ti^{4+}-substitution cathodes, there are no sharp peaks in the *dQ/dV* plots of equal-valent Ti^{4+} substituted $Li_2Mn_{1-x}Ti_xO_3$ during the discharge process (Fig. S6 in Supporting infromation), demonstrating that the activation of $Mn^{3+/4+}$ redox is mainly contributed by the unequal substitution with interlayer Li vacancies.

The cycling performance of Li_2MnO_3 based cathodes was measured at a current density of 50 mA/g. As shown in Fig. 5a, the initial capacities of $Li_{0.5}[Li_{1/3}Mn_{2/3}]_{0.5}Ti_{0.5}O_2$, $Li_{0.7}[Li_{1/3}Mn_{2/3}]_{0.7}Ti_{0.3}O_2$, $Li_{0.9}[Li_{1/3}Mn_{2/3}]_{0.9}Ti_{0.1}O_2$, and Li_2MnO_3 cathodes are 220, 242, 143 and 167 mAh/g, respectively, and their capacity retention after 60 cycles are 59%, 83%, 84%, and 39%, respectively. $Li_2Mn_{0.9}Ti_{0.1}O_3$ and $Li_2Mn_{0.7}Ti_{0.3}O_3$ cathodes have 139 and 143 mAh/g capacities with 47% and 61% retentions at 50 mA/g after 60 cycles (Fig. S7 in Supporting information). Among these cathodes, $Li_{0.7}[Li_{1/3}Mn_{2/3}]_{0.7}Ti_{0.3}O_2$ cathode shows the highest CE in 60 cycles, especially in the first five cycles (Fig. S8 in Supporting information). In view of these results, the unequal-valent Ti^{4+}-substitution with interlayer Li vacancies building and Ti^{4+}-substitution can increase capacities and improve cyclic stability of Li_2MnO_3 based cathodes. In addition, $Li_{0.7}[Li_{1/3}Mn_{2/3}]_{0.7}Ti_{0.3}O_2$ cathode delivers a high energy of 661 Wh/kg (457 Wh/kg for Li_2MnO_3) and a residual energy of 447 Wh/kg (144 Wh/kg for Li_2MnO_3) after 60 cycles (Fig. 5b and Fig. S9 in Supporting information). The rate ability of $Li_{1-x}[Li_{1/3}Mn_{2/3}]_{1-x}Ti_xO_2$ ($x = 0$, 0.1, 0.3 and 0.5) cathodes also was investigated. The rate performance of Li_2MnO_3 cathode is enhanced with the appropriate unequal-valent Ti^{4+}-substitution (Fig. 5c), implying that Ti^{4+} substitution and interlayer Li vacancies induce a thermodynamically fast Li-ion intercalation process in the Li_2MnO_3 structural phase.

DFT calculations (Fig. 6) in terms of structural relaxation and total energy were carried out to further understand the improved LIBs performance of the modified Li_2MnO_3 cathodes. The simplified model of Ti replacing Mn is adopted to show the effect of Ti^{4+} substitution in Li_2MnO_3. Calculation results show that the aver-

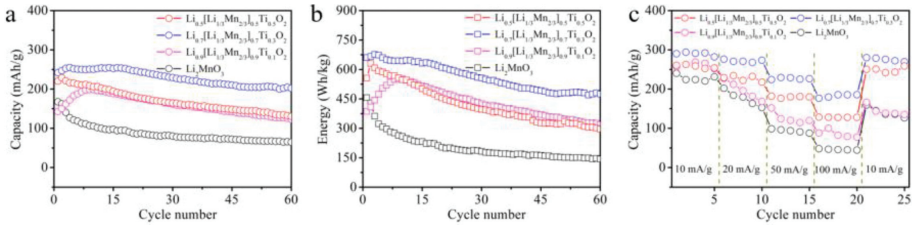

Fig. 5. (a) Capacity, (b) energy density, and (c) rate performance of the $Li_{1-x}[Li_{1/3}Mn_{2/3}]_{1-x}Ti_xO_2$ ($x = 0$, 0.1, 0.3 and 0.5) at a current density of 50 mA/g.

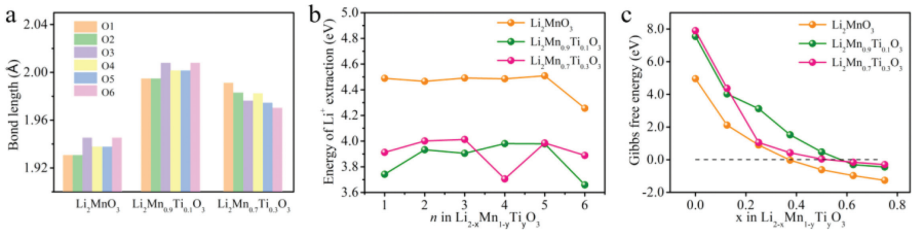

Fig. 6. (a) Calculated bond length of TM-O between oxygen and transition metals in Li_2MnO_3, $Li_2Mn_{0.9}Ti_{0.1}O_3$ and $Li_2Mn_{0.7}Ti_{0.3}O_3$, respectively. (b) Calculated formation energies of Li vacancies in Li_2MnO_3, $Li_2Mn_{0.9}Ti_{0.1}O_3$ and $Li_2Mn_{0.7}Ti_{0.3}O_3$. (c) Calculated reaction Gibbs free energy of O_2 release from the lattice of $Li_{2-x}Mn_{1-y}Ti_yO_3$, with $x = 0$, 0.125, 0.25, 0.375, 0.5, 0.625, 0.75, and $y = 0$, 0.1, 0.3.

age length of the TM–O bond increased compared to the length of the Mn–O bond in Li_2MnO_3 after Ti^{4+} substitution ($Li_2Mn_{0.9}Ti_{0.1}O_3$ and $Li_2Mn_{0.7}Ti_{0.3}O_3$) (Fig. 6a). O1-O6 stand for six TM–O bonds in [TMO_6] octahedron as shown in Fig. S10 (Supporting information). In addition, the substitution of Ti^{4+} pushes the surrounding atoms away from the [TiO_6] octahedron, which is consistent with the Mo doped Li_2MnO_3 configuration [47], indicating that the surrounding structure is loose. For the $Li_2Mn_{0.9}Ti_{0.1}O_3$ and $Li_2Mn_{0.7}Ti_{0.3}O_3$ structures, the calculated supercell volume will increase from 413.5 $Å^3$ to 418.0 $Å^3$ and 417.7 $Å^3$, respectively, as listed in Table S2 (Supporting information). According to Gao *et al.* [47], the expanded lattice due to Ti doping can facilitate the Li-ion diffusion. The correlations between the delithiation energy and the lithium content under different substitution conditions are shown in Fig. 6b, where n represents the number of Li-ions extraction. With respect to the pristine Li_2MnO_3, the delithiation energy is reduced by 0.58–0.75 eV after the Ti^{4+} substitution, indicating that the electrochemical activity of Li_2MnO_3 is enhanced by the incorporation of Ti^{4+}.

Furthermore, we evaluate the O_2 release reaction to reflect the stability of the oxygen sublattice in Ti^{4+} substituted Li_2MnO_3 using DFT calculations. Considering the entropy of gas phase O_2 under standard states ($-T\Delta S = -0.63$ eV) [48], the Gibbs free energy ΔG can be obtained. Fig. 6c shows the reaction Gibbs free energy of O_2 release from the lattice of $Li_{2-x}Mn_{1-y}Ti_yO_3$. Upon delithiation, the Gibbs free energies decrease monotonically, indicating that the lattice stability of $Li_{2-x}Mn_{1-y}Ti_yO_3$ will decrease with increasing amount of delithiation. In the case of unsubstituted Li_2MnO_3, the formation Gibbs energy is below zero when $x > 0.4$, indicating that the oxygen release reaction would occur spontaneously. After Ti doping, the spontaneous oxygen release will delay to $x > 0.5$ and $x > 0.6$ for $Li_2Mn_{0.7}Ti_{0.3}O_3$ and $Li_2Mn_{0.9}Ti_{0.1}O_3$, respectively, suggesting that the O_2 release reaction is suppressed and consequently the structural stability is improved.

We carried out *ex-situ* XRD measurement to detect the structural evolution of $Li_{0.7}[Li_{1/3}Mn_{2/3}]_{0.7}Ti_{0.3}O_2$ and Li_2MnO_3 at open circuit (OC), full charge (FC) and full discharge (FD) states under a current density of 10 mA/g. The *ex-situ* XRD patterns are shown in Figs. 7a and b. At the first FC state, the diffraction peak of (001) slightly shifts to high degree (clearly shown in Fig. S11a in Supporting information) in $Li_{0.7}[Li_{1/3}Mn_{2/3}]_{0.7}Ti_{0.3}O_2$ due to the lattice oxygen oxidation with Li^+ removing from TM layer. On contrast, the (001) diffraction peak of Li_2MnO_3 shifts to low degree at initial FC state (Fig. S11b in Supporting information), indicating the enlarging of the interlayer spacing caused by the excessive lattice oxygen dimerization and the oxygen release, which represents an unstable structure during the charge process. At the initial FD state, the interlayer spacing of both $Li_{0.7}[Li_{1/3}Mn_{2/3}]_{0.7}Ti_{0.3}O_2$ and Li_2MnO_3 becomes large due to Li^+ intercalation, which is a typical lithiation phenomenon in layered oxide cathodes. The (001) diffraction peak of $Li_{0.7}[Li_{1/3}Mn_{2/3}]_{0.7}Ti_{0.3}O_2$ moves back, which means that $Li_{0.7}[Li_{1/3}Mn_{2/3}]_{0.7}Ti_{0.3}O_2$ with enlarged interlayer spacing can alleviate the strain perpendicular to z axis during Li^+ intercalation. It avoids the lattice collapse in layered structure. Differently, the (130) diffraction peak of FD state in $Li_{0.7}[Li_{1/3}Mn_{2/3}]_{0.7}Ti_{0.3}O_2$ disappears, which means that the Mn^{4+} reduction induced extra embedded Li^+ are not arranged as regularly as Li^+ in Li_2MnO_3. The extra Li^+ intercalation exhibits a good reversible behavior as the (130) diffraction peak reappears in $Li_{0.7}[Li_{1/3}Mn_{2/3}]_{0.7}Ti_{0.3}O_2$ electrode at the second FC state.

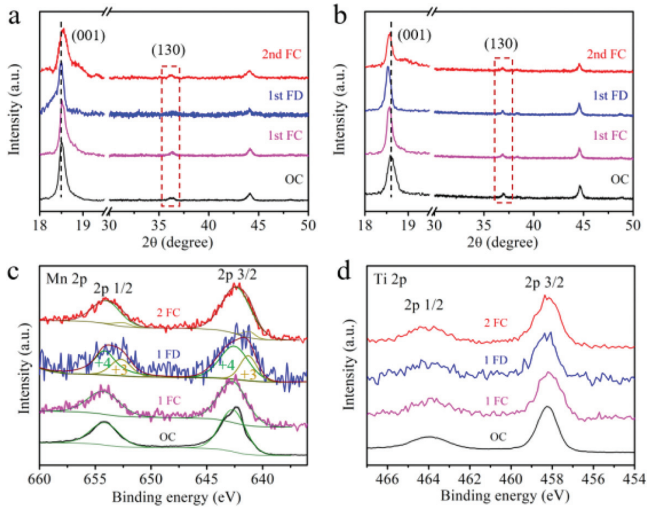

Fig. 7. *Ex-situ* XRD patterns of (a) $Li_{0.7}[Li_{1/3}Mn_{2/3}]_{0.7}Ti_{0.3}O_2$ and (b) Li_2MnO_3 cathodes. And *ex-situ* XPS spectra of the $Li_{0.7}[Li_{1/3}Mn_{2/3}]_{0.7}Ti_{0.3}O_2$ electrode for (c) Mn and (d) Ti elements.

Furthermore, the *ex-situ* XPS tests were taken out to analyze the charge compensation mechanisms and identify the source of the increased capacity. Fig. 7c shows the *ex-situ* XPS spectra of Mn element in $Li_{0.7}[Li_{1/3}Mn_{2/3}]_{0.7}Ti_{0.3}O_2$ at different states. Mn^{4+} is not oxidized to a high valence state during the charge process, while it is partially reduced to Mn^{3+} as expected with a Mn^{4+}/Mn^{3+} ions ratio of 2.2 (closing to the Li/V_{Li} ratio of 0.7/0.3 in lithium layer) in the first FD state. It can further confirm that the increased capacity is originate from the $Mn^{3+/4+}$ redox reaction. Subsequently, almost all of the Mn^{3+} are oxidized to Mn^{4+} at the second FC state, representing a good reversibility of the $Mn^{3+/4+}$ redox. The *ex-situ* XPS spectra of Ti element in $Li_{0.7}[Li_{1/3}Mn_{2/3}]_{0.7}Ti_{0.3}O_2$ are shown in Fig. 7d. Ti^{4+} always exists without charge transfer, further verifying the stable and inert of titanium in cathodes at high voltages, which is beneficial to improve the electrochemical stability of unequal-valent Ti^{4+}-substituted Li_2MnO_3 cathodes.

In summary, a series of unequal-valent Ti^{4+}-substituted Li_2MnO_3 ($Li_{1-x}[Li_{1/3}Mn_{2/3}]_{1-x}Ti_xO_2$, $x = 0$, 0.1, 0.3 and 0.5) samples are successfully designed. After unequal-valent Ti^{4+}-substitution, the interlayer Li vacancies are built. Our strategy can stabilize the structure and improve the cycling performance of Li_2MnO_3-based cathodes. In particular, the substitution of Ti^{4+} for Li^+ in TM layer leads to the formation of Li vacancies in lithium layer, which is in good agreement with the DFT calculation results that the Li vacancies preferentially existed at 2c and 4h sites (lithium layer) in Li_2MnO_3. The interlayer Li vacancies facilitate the Li-ion transport and greatly increase the capacity by activating the reversible $Mn^{3+/4+}$ redox during the charge/discharge processes. In addition, DFT calculations simultaneously confirm that the Ti^{4+} substituted Li_2MnO_3 can promote Li-ion diffusion and inhibit the oxidation of O^{2-} above 4.5 V. The as-designed $Li_{0.7}[Li_{1/3}Mn_{2/3}]_{0.7}Ti_{0.3}O_2$ cathode displays a high capacity of 290 mAh/g, stable cycling and enhanced rate performance. Therefore, the unequal-valent Ti^{4+}-substitution is an efficient strategy for improving the electrochemical performance of Li_2MnO_3.

Declaration of competing interest

There are no conflicts to declare.

Acknowledgments

This work was financially supported by the National Natural Science Foundation of China (Nos. 51972258 and 22109186) and Open Fund by Sanya Science and Education Innovation Park of Wuhan University of Technology (No. 2021KF0021). Y. Sun is supported by 21C Innovation Laboratory, Contemporary Amperex Technology Ltd. by Project No. 21C-OP-202002.

Supplementary materials

Supplementary material associated with this article can be found, in the online version, at doi:10.1016/j.cclet.2022.05.008.

References

[1] K. Shen, Z. Wang, Y. Ying, et al., Adv. Energy Mater. 9 (2019) 1900260.
[2] L.P. Wang, Z.R. Wu, J. Zou, et al., Joule 3 (2019) 2086–2102.
[3] P.K. Nayak, E.M. Erickson, F. Schipper, et al., Adv. Energy Mater. 8 (2018) 1702397.
[4] Y.X. Zuo, B. Li, N. Jiang, et al., Adv. Mater. 30 (2018) 1707255.
[5] J.R. Croy, M. Balasubramanian, K.G. Gallagher, A.K. Burrell, Acc. Chem. Res. 48 (2015) 2813–2821.
[6] S. Hy, H. Liu, M. Zhang, et al., Energy Environ. Sci. 9 (2016) 1931–1954.
[7] N. Guerrini, L. Jin, J.G. Lozano, et al., Chem. Mater. 32 (2020) 3733–3740.
[8] S.Q. Zhao, K. Yan, J.Q. Zhang, B. Sun, G.X. Wang, Angew. Chem. Int. Ed. 60 (2021) 2208–2220.
[9] X. Li, Y. Qian, S.H. Guo, et al., Adv. Mater. 30 (2018) 1705197.
[10] N. Li, J. Wu, S. Hwang, et al., ACS Energy Lett. 5 (2020) 3535–3543.
[11] L. Gu, D. Xiao, Y.S. Hu, H. Li, Y. Ikuhara, Adv. Mater. 27 (2015) 2134–2149.
[12] D.H. Seo, J. Lee, A. Urban, et al., Nat. Chem. 8 (2016) 692–697.
[13] J. Lee, D.H. Seo, M. Balasubramanian, et al., Energy Environ. Sci. 8 (2015) 3255–3265.
[14] W.E. Gent, K. Lim, Y. Liang, et al., Nat. Commun. 8 (2017) 2091.
[15] S.F. Li, Z.Y. Gu, J.Z. Guo, et al., J. Mater. Sci. Technol. 78 (2021) 176–182.
[16] Z.Y. Gu, J.Z. Guo, J.M. Cao, et al., Adv. Mater. 34 (2022) 2110108.
[17] M.Y. Wang, X.X. Zhao, J.Z. Guo, et al., Green Energy Environ. 7 (2022) 763–771.
[18] J. Song, B. Li, Y. Chen, et al., Adv. Mater. 32 (2020) 2000190.
[19] F. Ning, B. Li, J. Song, et al., Nat. Commun. 11 (2020) 4973.
[20] Z. Chen, Y. Qin, K. Amine, Y.K. Sun, J. Mater. Chem. 20 (2010) 7606–7612.
[21] F.D. Yu, L.F. Que, C.Y. Xu, et al., Nano Energy 59 (2019) 527–536.
[22] K. Kang, D. Carlier, J. Reed, et al., Chem. Mater. 15 (2003) 4503–4507.
[23] L. Xiao, J. Xiao, X.Q. Yu, et al., Nano Energy 16 (2015) 143–151.
[24] D.Y.W. Yu, K. Yanagida, Y. Kato, H. Nakamura, J. Electrochem. Soc. 156 (2009) A417.
[25] S.F. Amalraj, B. Markovsky, D. Sharon, et al., Electrochim. Acta 78 (2012) 32–39.
[26] S.H. Park, Y. Sato, J.K. Kim, Y.S. Lee, Mater. Chem. Phys. 102 (2007) 225–230.
[27] S.J. Kim, M.C. Kim, D.H. Kwak, et al., J. Power Sources 304 (2016) 119–129.
[28] Y. Kobayashi, M. Sawamura, S. Kondo, et al., Mater. Today 37 (2020) 43–55.
[29] D. Li, X. Zhang, X. Miao, et al., J. Alloy Compd. 797 (2019) 1258–1267.
[30] J. Lu, Q. Peng, W. Wang, et al., J. Am. Chem. Soc. 135 (2013) 1649–1652.
[31] F. Wu, T.P. Pollard, E. Zhao, et al., Energy Environ. Sci. 11 (2018) 807–817.
[32] L. Zhang, H. Noguchi, J. Electrochem. Soc. 150 (2003) A601.
[33] Y. Wang, X. Xiao, Q. Li, H. Pang, Small 14 (2018) 1802193.
[34] F. Li, X. Zhang, J. Lin, et al., J. Phys. Chem. C 123 (2019) 23403.
[35] P. Gao, Z. Chen, Y. Gong, et al., Adv. Energy Mater. 10 (2020) 1903780.
[36] R. Wang, X. He, L. He, et al., Adv. Energy Mater. 3 (2013) 1358–1367.
[37] Y. Koyama, I. Tanaka, M. Nagao, R. Kanno, J. Power Sources 189 (2009) 798–801.
[38] G. Liang, Z. Wu, C. Didier, et al., Angew. Chem. Int. Ed. 59 (2020) 10594–10602.
[39] D. Luo, S.H. Fang, Q.H. Tian, et al., Nano Energy 21 (2016) 198–208.
[40] S. Komaba, N. Yabuuchi, S. Ikemoto, J. Solid State Chem. 183 (2010) 234–241.
[41] X. Zhang, J. Shi, J. Liang, et al., Adv. Mater. 30 (2018) 1801751.
[42] C.M. Julien, M. Massot, Mater. Sci. Eng. B 100 (2003) 69–78.
[43] X.K. Ding, D. Luo, J.X. Cui, et al., Angew. Chem. Int. Ed. 59 (2020) 7778–7782.
[44] D.Y.W. Yu, K. Yanagida, H. Nakamura, J. Electrochem. Soc. 157 (2010) A1177.
[45] J.Q. Zhao, R.M. Huang, W.P. Gao, et al., Adv. Energy Mater. 5 (2015) 1401937.
[46] P. Lanz, C. Villevieille, P. Novák, Electrochim. Acta 130 (2014) 206–212.
[47] Y. Gao, J. Ma, X. Wang, et al., J. Mater. Chem. A 2 (2014) 4811–4818.
[48] J.S. Hummelshøj, J. Blomqvist, S. Datta, et al., J. Chem. Phys. 132 (2010) 071101.